Microsc. Microanal. 18, 1362–1367, 2012
doi:10.1017/S1431927612013530

Microscopy AND Microanalysis

Three-Dimensional Characterization of Iron Oxide (α-Fe_2O_3) Nanoparticles: Application of a Compressed Sensing Inspired Reconstruction Algorithm to Electron Tomography

Niven Monsegue,[1,*] Xin Jin,[2,3] Takuya Echigo,[4,5,†] Ge Wang,[2] and Mitsuhiro Murayama[1,6]

[1]*Institute for Critical Technology and Applied Science, Virginia Tech, Blacksburg, VA 24061, USA*
[2]*School of Biomedical Engineering & Sciences, Virginia Tech, Blacksburg, VA 24061, USA*
[3]*Department of Engineering Physics, Tsinghua University, Beijing 100084, China*
[4]*Center for NanoBioEarth, Department of Geosciences, Virginia Tech, Blacksburg, VA 24061, USA*
[5]*Japan International Research Center for Agricultural Sciences, Ohwashi 1-1, Tsukuba 305-8686, Ibaraki, Japan*
[6]*Department of Materials Science and Engineering, Virginia Tech, Blacksburg, VA 24061, USA*

Abstract: In this article, we demonstrate the application of a new compressed sensing three-dimensional reconstruction algorithm for electron tomography that increases the accuracy of morphological characterization of nanostructured materials such as nanocrystalline iron oxide particles. A powerful feature of the algorithm is an anisotropic total variation norm for the L1 minimization during algebraic reconstruction that effectively reduces the elongation artifacts caused by limited angle sampling during electron tomography. The algorithm provides faithful morphologies that have not been feasible with existing techniques.

Key words: computed tomography, STEM, compressed sensing, 3D reconstruction, quantification

Introduction

In electron tomography (ET), it is widely accepted that the quality of the final three-dimensional (3D) reconstructed image is directly related to the number of projections acquired and their angular range (Midgley & Weyland, 2003; Kawase et al., 2007). This is especially true for the widely used commercial reconstruction algorithms, i.e., back projection (BP), weighted back projection (WBP), and simultaneous iterative reconstruction technique (SIRT); these algorithms are well suited for ideal applications where there are a large number of projection images and a 360° range of projections (or from −90° to 90° viewing angles). Several studies have shown two major problems in a practical ET: (1) the reconstruction resolution decreases as the number of projections decreases, and (2) the limited angular range produces a missing wedge of information that blurs and elongates the reconstructed object parallel to the optical axis of the instrument (Weyland, 2002; Midgley & Weyland, 2003).

In this article, we demonstrate a compressed sensing (CS) 3D reconstruction algorithm that works well with reduced datasets and substantially reduces missing wedge artifacts. These features make it a useful approach for minimizing beam damage, minimizing contamination, and for obtaining reliable spatial measurements from tomograms. CS aims to reconstruct signals and images from fewer measurements than were traditionally thought necessary (Candes et al., 2006; Donoho, 2006). A successful application of CS requires three criteria to be met: (1) transform sparsity, which means the desired image should have a sparse representation in a known transform domain, i.e., it must be compressible by transform coding; (2) incoherence of undersampling artifacts, which means the artifacts in linear reconstruction caused by undersampled data acquisition should be incoherent (noise-like) in the sparsifying transform domain; and (3) nonlinear reconstruction, which means the image should be constructed by a nonlinear method that enforces both sparsity of the image representation and consistency of the reconstruction with the acquired samples (Lustig et al., 2007).

In algebraic reconstruction algorithms such as SIRT, algebraic reconstruction technique (ART), and simultaneous algebraic reconstruction technique (SART), an object may be reconstructed from its projections by solving a system of linear equations as illustrated in Figure 1. This system of linear equations may be simply expressed as:

$$AX = P. \tag{1}$$

As illustrated in Figure 1, an object may be separated into discrete areas using a square grid and lines passing through this square grid are defined as rays. The components of A, $(a_{i,j})$ are the weighted contribution of the line segment of the i'th ray with respect to j'th square, $X(x_j)$. The projection, $P(p_1, p_2, p_3, \ldots, p_i)$, is then the ray summation of the contributions from X and A. Because the P and A quantities in equation (1) are known, the task of algebraic reconstruction techniques is to solve the inverse problem associated with equation (1); i.e., to use $A^{-1}P$ to find the

Received December 17, 2011; accepted May 8, 2012
*Corresponding author. E-mail: nmonsegu@vt.edu
†Present address: Functional Geomaterials Group, Environmental Remediation Materials Unit, National Institute for Materials Science, Namiki 1-1, Tsukuba, Ibaraki 305-0044, Japan

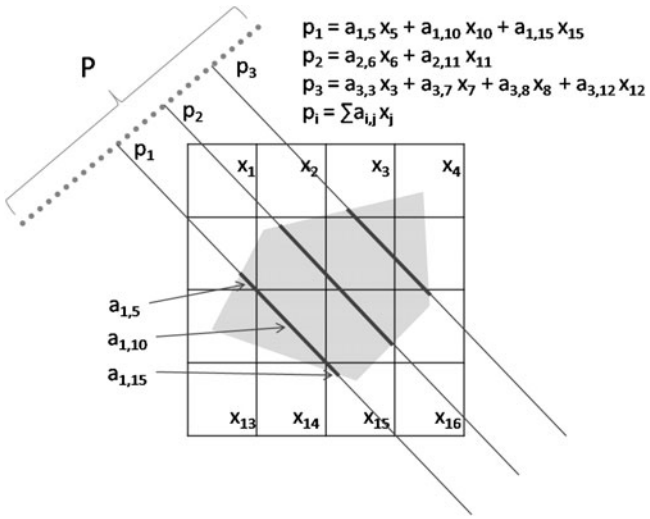

Figure 1. An illustration of the ray diagram used for creating a system of linear equations used in algebraic reconstruction techniques.

object, *X*. If a projected image *P* is sparseless and undersampled (as in the case of tomography), then *X* contains several components (unknowns) and the system of linear equations contains an infinite number of solutions. However, through CS the projected image is given a sparse representation thereby reducing the number of components in *P*; this improves the algebraic reconstruction algorithm's calculation of a best solution for the system of linear equations. Therefore, CS allows algebraic reconstruction algorithms to converge faster and more accurately to values of the true object. It should be noted that the result of CS is a piecewise constant. For that reason, if an object to be reconstructed can be described as a piecewise constant, as in many inorganic and organic materials in electron microscopy, then the CS algorithm will be effective. For ET, the theoretical basis and simulated application of CS to ET has been demonstrated by Binev et al. (2011). Binev's work examined CS's potential in both image collection and image recovery with particular attention to scanning transmission electron microscopy (STEM) imaging. Recently, Saghi et al. (2011) and Goris et al. (2012) have shown that the experimental application of CS to ET is indeed possible. Furthermore, Saghi's work also shows that CS is effective at reconstructing 3D maps with as few as nine tilt images.

The total variation method (TV) is derived from sparse signal recovery as seen in CS. Candes et al. (2006) indicated that medical computed tomography (CT) images could be approximately sparse by taking the magnitude of the gradient of these images. Based on this assumption, a total variation regularization reconstruction method was proposed that recovers CT images using incomplete samples in two-dimensional (2D) Fourier space. Recently it was proposed that an anisotropic total variation norm for the L1 minimization during algebraic reconstruction technique iterations may be more efficient than the standard total variation norm (Xin et al., 2010). The common approach to image CS through TV is achieved by performing L1 normalization on a gradient image as shown by equations (2) and (3):

$$|\nabla f_{x,y}| = \sqrt{(D_x f_{x,y})^2 + (D_y f_{x,y})^2}, \quad (2)$$

$$\nabla f = (D_x f, D_y f), \quad (3)$$

where $f_{x,y}$ is the image function, and D_x and D_y are discrete differential operators. In equation (2), the image gradient is used for edge preservation and the L1 normalization transform is used to create image sparsity. In this form, TV is isotropic in nature because both *x* and *y* directions have equal contributions in transforming the image. However, in limited angle reconstructions, artifacts and blurring occur due to the missing wedge of information. An improved method for dealing with limited angle reconstruction artifacts is to reduce the contributions to the L1 norm from the missing wedge direction while maintaining the contributions from other directions. This is done by modifying the calculation of the gradient image as shown by:

$$|\nabla_{A,B} f_{x,y}| = \sqrt{A(D_x f_{x,y})^2 + B(D_y f_{x,y})^2}, \quad (4)$$

where *A* and *B* are weighted parameters that are positive real numbers. When *A* and *B* are unequal, the TV method becomes anisotropic and we refer to this as anisotropic total variation (ATV). Based on this modification, a new ART + ATV reconstruction method for limited-angle problems was developed (Wang & Yu, 2010; Xin et al., 2010). The main principle of this method is to limit edge detection from radial directions that are blurred because of the missing angular range of projection views. As a result, edges from other radial directions can be better preserved.

In this work, we demonstrate that using a compressed sensing anisotropic total variation algebraic reconstruction technique (CSATV—application of the ART + ATV algorithm to ET) on reduced datasets of iron oxide nanoparticle images can maintain excellent overall 3D reconstruction quality while reducing missing wedge artifacts. A comparison of CSATV to BP, WBP, and SIRT examines the algorithm's performance when using images that contain a relatively low signal-to-noise ratio and a reduced number of projections. The factors governing each algorithm's performance are the sample's reconstruction geometry and surface characteristics. Furthermore, a quantitative comparison will be made between CSATV and SIRT with respect to the reconstructed object's length, surface area, and volume.

Materials and Methods

Iron oxide nanoparticles examined in this study were synthesized by forced hydrolysis of an acidic ferric nitrate solution (Fischer & Schwertmann, 1975; Schwertmann & Murad, 1983). Electron tomography was performed with a FEI Titan 80-300 (FEI Company, Hillsboro, OR, USA) transmission electron microscopy (TEM) operated at 200 kV. Iron oxide nanoparticles were held on a double film (ultrathin continuous carbon film reinforced by lacey carbon layer) coated copper grid (Cu-200HD, Pacific Grid-Tech, San Francisco, CA, USA). Tilt series were acquired in the

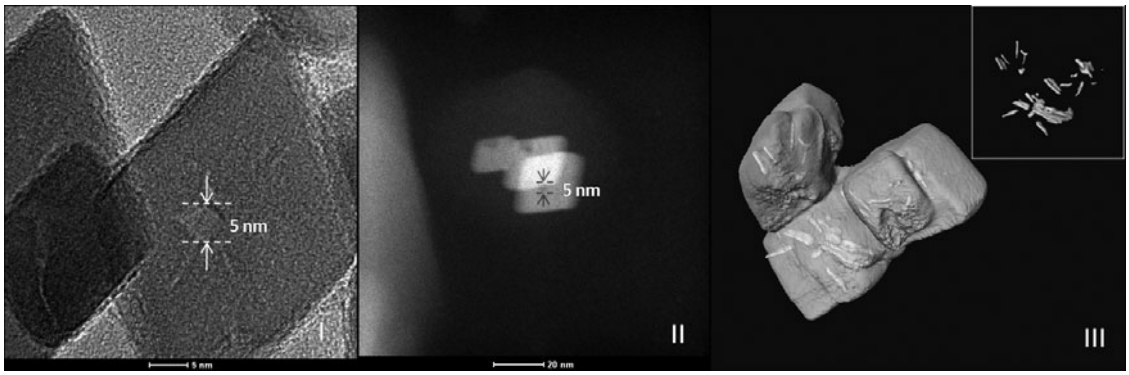

Figure 2. Micrographs of iron oxide nanoparticles displaying nanopores and nanopipes by (**I**) HRTEM, (**II**) STEM, and (**III**) isosurface rendering of SIRT reconstruction (the inset shows the distribution of nanopipes and nanopores within the iron oxide crystals).

high-angle annular dark-field (HAADF)-STEM mode using a Fischione Model 3000 (E.A. Fischione Instruments, Inc., Export, PA, USA) annular dark-field (ADF) detector with a beam convergence angle (semiangle) of 10.5 mrad and an ADF inner collection angle of 14.3 mrad. A Fischione 2020 ultrahigh-tilt single-axis tomography holder was used. Images were recorded every 1° in the tilt range of −65° to +65°. Following the acquisition of a tilt series, images were spatially aligned by a cross-correlation algorithm using the FEI Inspect 3D Xpress software package. BP, WBP, and SIRT reconstructions were also performed using FEI Inspect 3D Xpress. Dataset reduction was done by removing the appropriate projection angle images of the originally acquired tilt series, thus creating to a dataset consisting of 43 projection images from −63° to +63° with 3° increments. CSATV reconstruction was performed using code developed for MATLAB. Three-dimensional visualization, surface area, and volume measurements were performed using FEI Resolve RT (Amira 5.2.2). For surface area and volume measurements, reconstructed data were the first threshold using the Otsu thresholding algorithm implemented in FEI Resolve RT. The Otsu thresholding algorithm automatically selects an optimal threshold value based on discriminant analysis of an image's gray level histogram (Otsu, 1979); thus in this work, Otsu thresholding was performed after each reconstruction (BP, WBP, SIRT, and CSATV) to obtain an objective threshold value for comparing reconstruction techniques.

Results

A typical high-resolution TEM (HRTEM) image of an iron oxide nanoparticle synthesized by forced hydrolysis is shown in Figure 2(I). Facets of this particle are seen to create a rhombohedra shape, which is consistent for particles synthesized by this method (Rodriguez et al., 2007). Circular features approximately 5 nm in size appear at the center of these particles. Additionally, several lines appear to extend radially from the center of this particle. To obtain additional information on the internal features seen in the iron oxide nanoparticles, STEM-HAADF was used to determine if the features observed in the HRTEM image were due to a fluctuation of local bulk density. Figure 2(II) shows circular and linear features of the same dimensions as those seen in HRTEM. A halo of contamination over the field of view is also visible; the impact of this contamination will be discussed later. Since no other phase formation is likely due to the synthesis method used here, it is reasonable to conclude that these features are nanoscale cavities and channels. However, with 2D images it is difficult to interpret the morphology and exact geometrical location of these features in nanoparticles.

ET in the STEM-HAADF mode was performed on iron oxide nanoparticles to map in 3D both the surface morphology and the observed features seen in HRTEM and STEM-HAADF images. By examining slices of this 3D map and selecting features based on contrast, a network of internal features was generated. Figure 2(III) shows an isosurface rendering of a SIRT reconstruction of an iron oxide nanoparticle containing nanoscale pipes and cavities (internal light shading). Figure 2(III) inset shows the nanoscale pipes and cavities excluding the isosurface rendering of the iron oxide nanoparticle. From the inset image it is clear that a network is formed between the nanoscale pipes and cavities. A paper discussing the formation of these features has been accepted recently (Echigo et al., forthcoming).

It must be noted that selection of these internal features by automated thresholding proved unreliable due to the quality of the SIRT reconstruction as a result of image blurring caused by the contamination build up during the tomography tilt series acquisition.

Figures 3(I)–3(IV) are a comparison of orthoslice views in the *y*-*z* plane (the *z* axis is parallel to the electron beam) of BP, WBP, SIRT, and CSATV reconstructions using a reduced dataset of 43 images. In both BP (I) and WBP (II), substantial degradation in reconstruction quality is observed. The reconstructed surfaces of these nanoparticles appear coarse, and an overall elongation is observed parallel to the *z* axis. Additionally, there are significant noise-like artifacts present in the surroundings of the reconstructed object. Figure 3(III) is a SIRT reconstruction of the iron oxide nanoparticles. Here significant improvement is made to the overall geometry and surface reconstruction of the

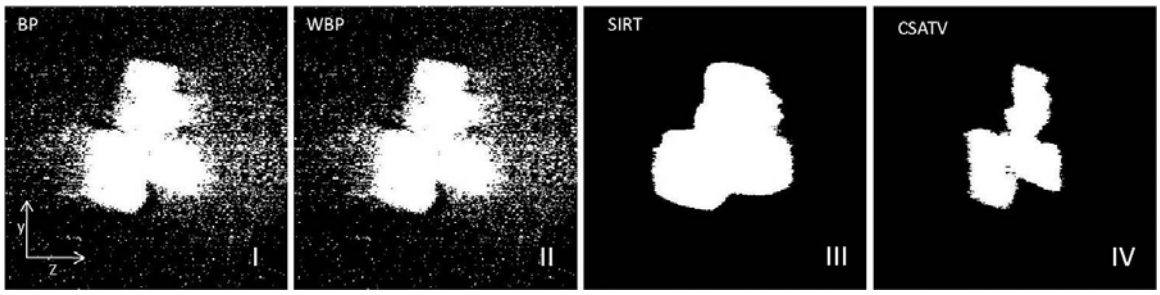

Figure 3. Orthogonal slices in the *y*-*z* plane of iron oxide nanoparticles by (**I**) BP, (**II**) WBP, (**III**) SIRT, and (**IV**) CSATV reconstructions. These images use Otsu's thresholding on the reconstructed data thereby creating an objective comparison.

iron oxide nanoparticle, and at the same time noise-like artifacts surrounding the nanoparticles have been removed. Surfaces in the SIRT reconstruction appear smooth and well defined compared to those of BP and WBP reconstructions; however, significant rounding has been produced in the iron oxide nanoparticle's facets. A CSATV reconstruction of the iron oxide nanoparticles is shown in Figure 3(IV). Compared to the SIRT reconstruction, the rhombohedra facets appear straight as opposed to the rounded appearance in the previous techniques. Unlike BP, WBP, and SIRT, the overall length of the CSATV reconstruction of the iron oxide nanoparticles in the *z* direction does not appear significantly elongated. Furthermore, cavity cross sections are now clearly observed intersecting the rhombohedra facet surface in the CSATV reconstruction. A complete 3D side-by-side isosurface rendering comparison of CSATV (green) and SIRT (yellow) iron oxide reconstructions is shown in Supplementary Movie 1.

Supplementary Movie 1

Supplementary Movie 1, which shows a tomogram of iron oxide nanoparticles, can be found online. Please visit journals.cambridge.org/jid_MAM.

To quantify the distortion in the *z* direction observed in the SIRT reconstruction and verify the overall accuracy of CSATV reconstruction, SIRT and CSATV iron oxide nanoparticles reconstructed from the reduced dataset were compared to the STEM-HAADF images of the original tilt series. Figure 4(I) shows a STEM-HAADF image of the iron oxide nanoparticles at 0° tilt. For clarity, Otsu thresholding has been performed on the STEM-HAADF images to remove background effects [Fig. 4(II)]. The corresponding SIRT and CSATV reconstruction images are shown in Figures 4(III) and 4(IV), respectively. Quantification of each reconstruction algorithm's accuracy was done by plotting the pixel values across the line A-B then comparing this plot to the corresponding STEM-HAADF with Otsu thresholding image [Fig. 4(V)]. Figures 5(I)–5(IV) show a rotation of 65° tilt in the iron oxide nanoparticles and the respective rotations in SIRT and CSATV images.

Table 1 is a summary of the measurements obtained from Figures 4 and 5. For 0° tilt, both the STEM-HAADF and CSATV images are 42 nm in length while the SIRT reconstructed image is 46 nm. At 65° tilt, the STEM-HAADF and CSATV reconstruction lengths are 44 and 46 nm, respectively. In contrast, the length measured for the SIRT reconstructed image is 65 nm. Differences in surface area and volume were also compared between CSATV and SIRT reconstructed iron oxide nanoparticles; however, these measurements were not compared to the corresponding STEM-HAADF image because this measurement requires a full 360° of projections to calculate surface area and volume accurately. A volume increase of approximately 100% is observed in iron oxide nanoparticles reconstructed by SIRT compared to that of the CSATV reconstruction. At the same time, the surface areas of SIRT and CSATV reconstructed iron oxide nanoparticles are approximately the same. This similarity in surface area is the due to the missing internal features (cavities and nanopipes) in the SIRT reconstruction. Figures 6(I) and 6(II) show a comparison of SIRT and CSATV reconstructions using the same orthoslice position in each iron oxide nanoparticle. In the CSATV reconstruction a cavity is observed while there is no cavity in the SIRT reconstruction.

Discussion

It is useful when analyzing the performance of CSATV to begin by examining the dataset used for the current comparison. As shown in Figure 2(II), a buildup of carbon contamination occurs during the tilt series acquisition. As a result, image quality has been greatly reduced. In addition, the automated focusing system, which relies on image contrast to calculate an appropriate defocus, suffered inconsistencies

Table 1. A Comparison of Iron Oxide Nanoparticle Dimension (Figs. 3 and 4, line A-B) for STEM and Otsu Thresholding, CSATV, and SIRT at 0° and 65° Tilts.*

	Length at 0° (nm)	Length at 65° (nm)	Surface Area (nm^2)	Volume (nm^3)
STEM	42	44	—	—
CSATV	42	46	13,237	34,648
SIRT	46	65	13,268	69,767

*Surface area and volume comparisons were made for CSATV and SIRT only.

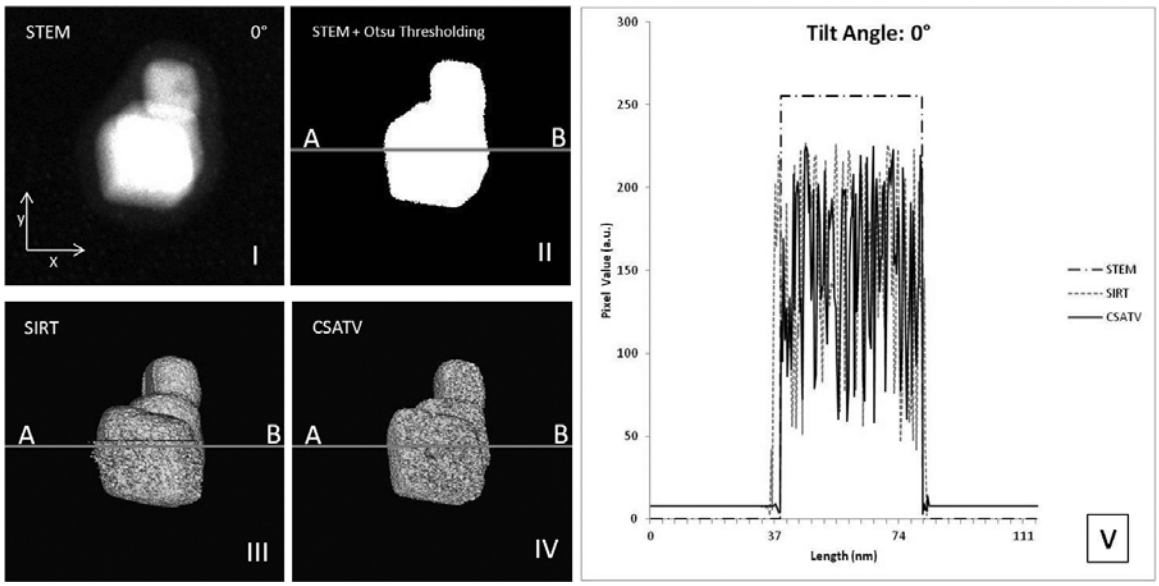

Figure 4. Comparison of iron oxide nanoparticle images by (**I**) STEM, (**II**) STEM and Otsu thresholding, (**III**) CSATV, and (**IV**) SIRT at 0° tilt. The line A-B is the location where a pixel intensity line profile plot was measured in each image and shown in the respective plot (**V**).

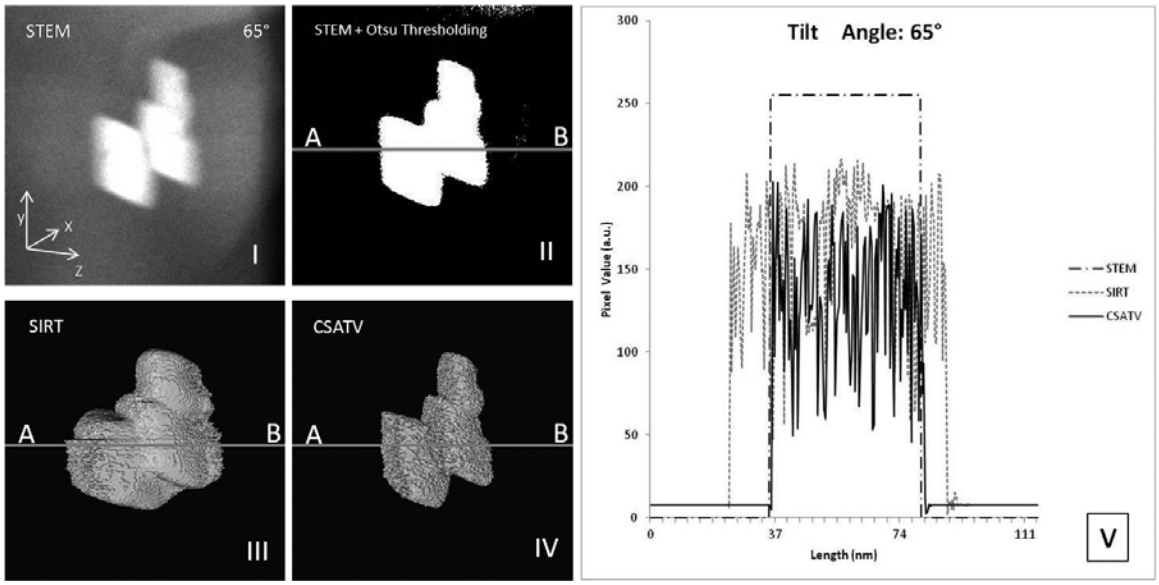

Figure 5. Comparison of iron oxide nanoparticle images by (**I**) STEM, (**II**) STEM and Otsu thresholding, (**III**) CSATV, and (**IV**) SIRT at 65° tilt. The line A-B is the location where a pixel intensity line profile plot was measured in each image and shown in the respective plot (**V**).

due to the reduced contrast caused by carbon contamination; hence, focus quality was poor for some tilt angle images. The combination of these issues would explain the very low reconstruction quality of BP and WBP, as well as the bloated, rounded appearance of iron oxide nanoparticles reconstructed by SIRT. Despite the presence of contamination and poor focus quality in some of the tilt series images, CSATV has reconstructed iron oxide nanoparticles to a significantly improved accuracy compared to SIRT. Another area of improvement has been the reduction of the missing wedge artifact. In this comparison it is clear that CSATV has greatly reduced the elongation caused by the missing wedge of information. With respect to surface area and volume, the large increase in volume by SIRT reconstruction is attributed to the elongation from the missing wedge effect; however, this volume increase may also be attributed to the missing cavities and nanopipes in the SIRT reconstruction. This suggests that reconstruction accuracy has been reduced due to both the reduction in the tomography dataset and the missing wedge artifact. In contrast, the CSATV algorithm is less prone to dataset reduction and the missing wedge artifact.

The advantages provided by CSATV are particularly useful for systems where high tilt angles and high electron

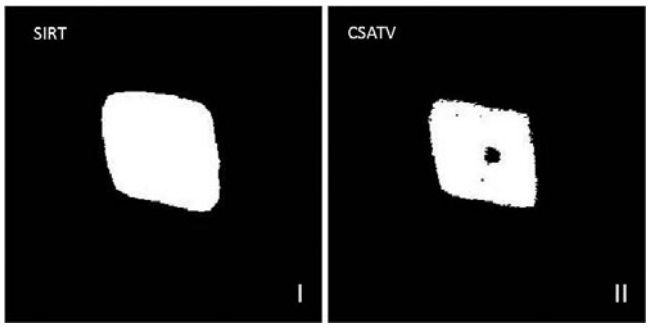

Figure 6. A comparison between (**I**) SIRT and (**II**) CSATV showing identical orthoslice positions. In the SIRT reconstructed orthoslice, no internal feature (cavity) is present. By comparison, an internal feature is observed in the CSATV reconstruction. These missing features in the SIRT reconstruction explain the reduced surface area measurement observed.

doses may not be feasible, yet a reasonably accurate tomogram is needed. Also, the study of various material morphologies such as catalyst particles, nanoscale pipes, and cavities will be greatly improved by the elongation error reduction offered by CSATV; the same is true for biological samples where structure analysis is key to understanding cell transformation and propagation (Kelly et al., 2007). Accurately quantifying the physical dimension of these features is an attractive application of ET. As is confirmed by the work of Saghi et al. (2011), the application of CS to ET is capable of more accurately representing object volumes with far fewer projection images compared to SIRT. A future strategy for electron tomography may very well include reduced datasets for the purposes of reduced electron dose thereby preserving samples while maintaining image quality.

Conclusion

In this article, we have demonstrated that CSATV reconstruction can greatly improve the quality and accuracy of tomograms using reduced datasets when compared to the common reconstruction techniques of BP, WBP, and SIRT. Object geometry and a reduction in the missing wedge artifact are all seen to improve with CSATV.

Acknowledgments

This work was conducted at the Nanoscale Characterization and Fabrication Laboratory at the Institute for Critical Technology and Applied Science, Virginia Tech. We would also like to acknowledge Deborah Aruguete and Michael Hochella for assisting in the synthesis of the iron oxide nanoparticles and valuable insight in the interpretation of the internal features observed in these particles, as well as William T. Reynolds for providing informative discussion on many areas of this project. The authors also wish to acknowledge support from the Advanced Combustion Team, Office of Research Development, the National Energy Technology Laboratory, U.S. Department of Energy (DOE), the DOE Grant DE-FG02-06ER15786, the Japan Society for the Promotion of Science, Research Fellowships for Young Scientists (PD20-1531), and the Japan Excellent Young Researcher Overseas Visit Program.

References

Binev, P., Dahmen, W., DeVore, R., Lamby, P., Savu, D. & Sharpley, R. (2011). Compressed sensing and electron microscopy. Technical Report. Aachen Institute for Advanced Study in Computational Engineering Science.

Candes, E.J., Romberg, J. & Tao, T. (2006). Robust uncertainty principles: Exact signal reconstruction from highly incomplete frequency information. *IEEE T Inf Theory* **52**(2), 489–509.

Donoho, D.L. (2006). Compressed sensing. *IEEE T Inf Theory* **52**(4), 1289–1306.

Echigo, T., Monsegue, N., Aruguete, D.M., Murayama, M. & Hochella, M.F., Jr. (forthcoming). Nanopores in hematite (α-Fe_2-O_3) nanocrystals observed by electron tomography. *Amer Miner* **98**(1). Available at http://dx.doi.org/10.2138/am.2013.4120.

Fischer, W.R. & Schwertmann, U. (1975). Formation of hematite from amorphous iron(III) hydroxide. *Clay Clay Miner* **23**(1), 33–37.

Goris, B., Van den Broek, W., Batenburg, K.J., Heidari Mezerji, H. & Bals, S. (2012). Electron tomography based on a total variation minimization reconstruction technique. *Ultramicroscopy* **113**, 120–130.

Kawase, N., Kato, M., Nishioka, H. & Jinnai, H. (2007). Transmission electron microtomography without the "missing wedge" for quantitative structural analysis. *Ultramicroscopy* **107**(1), 8–15.

Kelly, D.F., Lake, R.J., Walz, T. & Artavanis-Tsakonas, S. (2007). Conformational variability of the intracellular domain of Drosophila Notch and its interaction with Suppressor of Hairless. *Proc Natl Acad Sci USA* **104**(23), 9591–9596.

Lustig, M., Donoho, D. & Pauly, J.M. (2007). Sparse MRI: The application of compressed sensing for rapid MR imaging. *Magn Reson Med* **58**(6), 1182–1195.

Midgley, P.A. & Weyland, M. (2003). 3D electron microscopy in the physical sciences: The development of Z-contrast and EFTEM tomography. *Ultramicroscopy* **96**(3–4), 413–431.

Otsu, N. (1979). Threshold selection method from gray-level histograms. *IEEE T Syst Man Cybern* **9**(1), 62–66.

Rodriguez, R.D., Demaille, D., Lacaze, E., Jupille, J., Chaneac, C. & Jolivet, J.P. (2007). Rhombohedral shape of hematite nanocrystals synthesized via thermolysis of an additive-free ferric chloride solution. *J Phys Chem C* **111**, 16866–16870.

Saghi, Z., Holland, D.J., Leary, R., Falqui, A., Bertoni, G., Sederman, A.J., Gladden, L.F. & Midgley, P.A. (2011). Three-dimensional morphology of iron oxide nanoparticles with reactive concave surfaces. A compressed sensing-electron tomography (CS-ET) approach. *Nano Lett* **11**(11), 4666–4673.

Schwertmann, U. & Murad, E. (1983). Effect of pH on the formation of goethite and hematite from ferrihydrite. *Clay Clay Miner* **31**(4), 277–284.

Wang, G. & Yu, H.Y. (2010). Can interior tomography outperform lambda tomography? *Proc Natl Acad Sci USA* **107**(22), E92–E93.

Weyland, M. (2002). Electron tomography of catalysts. *Top Catal* **21**(4), 175–183.

Xin, J., Liang, L., Zhiqiang, C., Li, Z. & Yuxiang, X. (2010). Anisotropic total variation for limited-angle CT reconstruction. In *2010 IEEE Nuclear Science Symposium Conference Record (NSS/MIC)*, pp. 2232–2238.